An Aerial Robot Passively Transforming between Hovering and Forward Flight via Aerodynamically Bistable Structure

Ruihan Jia, Songnan Bai, Song Li, Fangzheng Wang, Hongqiang Wang, and Pakpong Chirarattananon

***Abstract*—With the ubiquitous deployment of drones in various fields, aircraft capable of both hovering and forward flight have garnered increasing attention due to their versatility and long-range cruising capability. Currently, these multimodal aerial vehicles are generally achieved by introducing additional actuators, which inevitably results in redundant mass, complex structures, and reduced flight efficiency. In this work, we propose a 39-g bimodal aerial robot equipped with only two propellers as actuators. The robot can cruise like a fixed-wing aircraft or hover in place through self revolving. The transition between its flight modes is achieved through the introduction of several passive morphing mechanisms and aerodynamically bistable structure. With only two rotors, the robot leverages aerodynamic loads on the wings to maintain its flight configuration. Strategic adjustment of propeller thrust enables seamless transition between forward flight and hovering modes. Extensive indoor and outdoor experiments demonstrate the robot's stable operation in both flight modes, with power loading of 10.24 g/W in forward flight and 7.11 g/W in hovering mode. The robot successfully performs mode transitions in a predictable and repeatable manner. This approach enables a structurally proficient solution for multimodal flight without the need for additional actuators.**

I. Introduction

Micro aerial vehicles (MAVs) have gained widespread deployment across various scenarios due to their versatility and ease of use. Among these, fixed-wing drones and rotary-wing aircraft each offer advantages tailored to specific flight tasks. Rotary-wing aircraft, for instance, are favored for their simple mechanical structure and mature control strategies, enabling precise control during low-speed flight and hovering. This makes them particularly well-suited for navigating complex environments such as indoor spaces or dense forests [1]–[4]. In contrast, fixed-wing drones are renowned for their superior aerodynamic efficiency, which supports high-speed cruising and extensive area coverage [5]–[7].

This work was supported in part by the Shenzhen-Hong Kong-Macau Science and Technology Project (Category C) (grant no. SGDX20220530111401009) and in part by the Research Grants Council of the Hong Kong Special Administrative Region of China (grant number CityU 11218022.)

Ruihan Jia, Songnan Bai, Song Li, Fangzheng Wang and Pakpong Chirarattananon are with the Department of Biomedical Engineering, City University of Hong Kong, Hong Kong SAR, China. Hongqiang Wang is with the Shenzhen Key Laboratory of Intelligent Robotics and Flexible Manufacturing Systems, Southern University of Science and Technology, Shenzhen 518055, China. Pakpong Chirarattananon is also with the Department of Mechanical Engineering and Centre for Nature-Inspired Engineering, City University of Hong Kong, Hong Kong SAR, China, and Department of Mechanical and Industrial Engineering, University of Toronto, Toronto, ON M5S 3G8, Canada. (Ruihan Jia and Songnan Bai are co-first authors.) (Corresponding author: Pakpong Chirarattananon, email: p.chirarattananon@utoronto.ca).

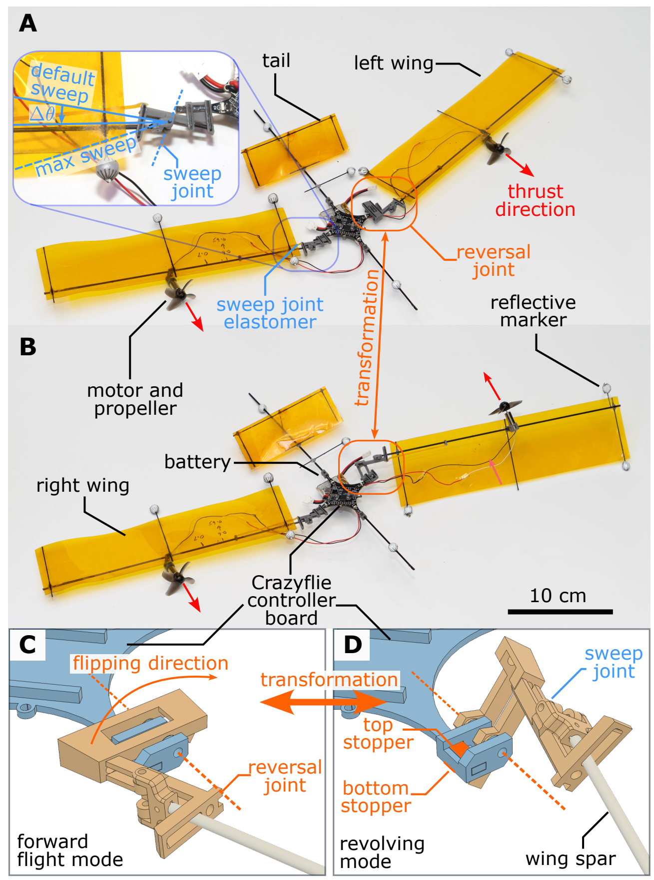

Fig. 1. Photos of the bimodal micro aerial robot. (A) The 39-gram vehicle in the forward flight mode. (B) The robot in the revolving mode. The closed-up view in (A) shows the passive variable-sweep mechanism. The bottom drawings illustrates the states of the wing reversal joint (located on the left wing). (C) Joint configuration in the forward flight mode. (D) Joint configuration in the revolving mode.

To expand operational capabilities and efficiency across different flight envelopes, morphing multimodal aerial robots have emerged as a significant asset for various applications. By modifying wing shape shape, size, or orientation, these robots are engineered to transition between flight modes [8]–[16], rather than being constrained to a single flight mode [2], [11], [17], [18]. This adaptability allows them to meet broader mission requirements. A prominent example of this trend is the emergence of Vertically Take-Off and Landing (VTOL) hybrid aerial robots, which combine hovering and forward flight modes within a single platform. These systems often incorporate morphing mechanisms to adjust the direction of thrust or alter the aerodynamic configuration, making them ideal for long-duration and long-distance missions [8], [19]–[24].

Beyond traditional fixed- and rotary-wing MAVs, revolving-wing aerial robots have emerged as a promising alternative, offering efficient hovering locomotion with low disk loading [15], [25]–[28]. Some of these designs exploit unsteady aerodynamics at high angles of attack (AoA) [26], [29], achieving up to twice the endurance and efficiency of other hover-capable aerial robots. Unlike rotorcraft, which use compact propellers for lift, revolving-wing robots generate lift via large aerodynamic surfaces, making them well-suited for transformation into fixed-wing drones through morphing [15], [16], [25].

While large multimodal MAVs can incorporate additional actuators, small aerial vehicles face severe constraints in weight, size, and actuator power, making it difficult to incorporate complex morphing mechanisms or extra actuators. To address this challenge, we introduce a novel passive morphing mechanism that enables a 39-gram robot to operate in both hovering and forward flight modes using only two propellers as illustrated in Fig. 1 and Supplementary Movie 1. The key innovation is a reversal joint on one wing, which serves as the primary morphing mechanism. Unlike conventional morphing designs that rely on active actuators, this free-to-rotate joint passively adapts to aerodynamic forces, exhibiting aerodynamic bistability. That is, the wing configuration remains stable in both flight modes under aerodynamic loading, eliminating the need for additional actuators. This differs from traditional bistable mechanisms that typically rely on elastic elements or compliant structures to create two stable states [10], [30], [31]. To enable flight mode transitions without additional actuators, we implement a passive variable-sweep mechanism [32] that allows interruption of aerodynamic stability simply by modulating the propeller thrust. This design enables multimodal flight with only two existing propellers, making it particularly suitable for resource-constrained small aerial vehicles.

II. Related Works

Multimodal MAVs are noted for their proficiency in both hovering and horizontal flight. These vehicles typically incorporate large aerodynamic surfaces, such as wings, and motor-driven propulsion systems. However, the complexity of their mechanical structures and functional requirements often results in larger sizes or increased weight. While extensive research has been conducted on multimodal MAVs [33], the focus has predominantly been on active morphing strategies. This section provides a comprehensive overview of current multimodal aerial vehicles, emphasizing actuation mechanisms, morphological transformations, and actuator configurations. We categorize these hybrid VTOL robots into four primary types, as depicted in Fig. 2, all of which share similar cruising capabilities but differ in their hovering mechanisms.

The most basic approach to VTOL drones involves (i) the direct integration of fixed-wing and rotorcraft configurations as illustrated in Fig. 2. This method leverages well-established

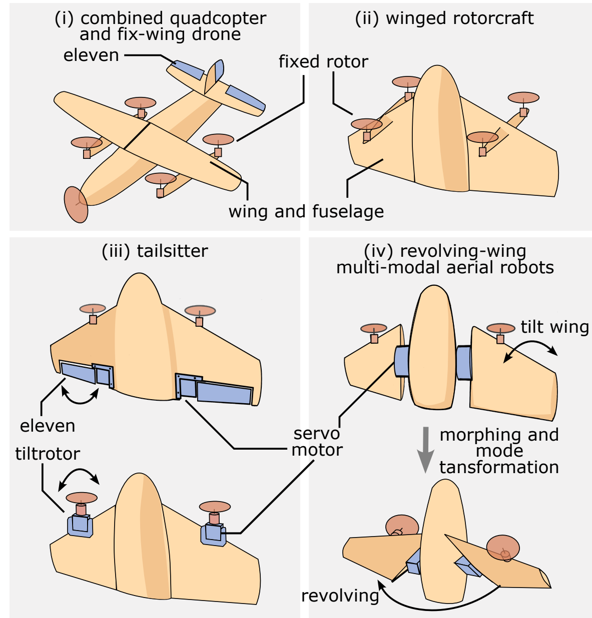

Fig. 2. Schematic diagrams of four types of hybrid VTOL MAVs. The body, actuators for propelling and actuators for control are in three different colors.

control strategies for both flight modes but often results in redundant propulsion and actuation systems, compromising overall flight efficiency [20]. Some designs have attempted to mitigate this issue by incorporating tiltable rotors [23], allowing shared propulsion across flight modes. However, this solution introduces additional complexity and non-propulsive actuators.

In an effort to streamline designs, researchers have explored (ii) the addition of vertically mounted wings to rotorcraft (Fig. 2). These "winged rotorcraft" [24], [31], [34], [35] benefit from simplified mechanical structures and control strategies, relying on differential propeller thrust for attitude control in both flight modes. However, the typically modest wing sizes limit aerodynamic efficiency during forward flight, and the lack of active aerodynamic surfaces results in insufficient roll control during forward flight [36].

To address these limitations, (iii) tailsitter configurations have been developed, incorporating active aerodynamic surfaces [19], [37]–[40]. These vehicles are typically equipped with only two propellers and two servo-driven elevons. They can takeoff and land with an upright attitude with the thrust pointing upward and transition to forward flight mode by pitching down to attain horizontal attitude, leveraging the wings for lift generation. Unlike winged rotorcraft, tailsitters generate roll and pitch torque via aerodynamic surfaces, resulting in more efficient attitude control in forward flight. An alternative tailsitter design employs two tiltable rotors [41] instead of elevons to achieve attitude control. In hovering mode, these vehicles are functionally identical to bicopters [42] with a simpler control strategy. However, they potentially sacrificing efficiency in forward flight due to the reliance on propeller thrust, instead of wings, for longitudinal stability [41].

While these VTOL designs effectively leverage fixed-wing

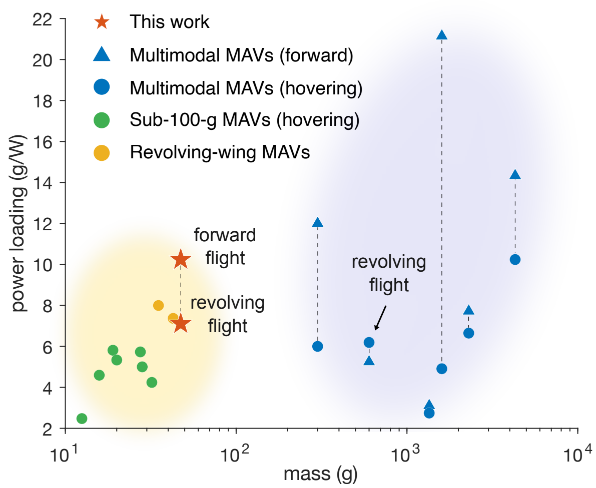

Fig. 3. Power loading versus mass of multimodal aerial robots capable of both hovering and forward flight, as well as lightweight MAVs. The dataset includes include samara-inspired MAVs (yellow) [26], hover-capable MAVs (green) [43]–[49], and multimodal MAVs (blue) [6], [31], [50]–[53]. Circular markers indicate hovering power loading and triangular markers represent forward flight power loading. Dashed lines connect data points for hybrid vehicles capable of both flight modes. Refer to Supplementary Table S1 for complete numerical data.

efficiency for extended flights, they often struggle with hovering efficiency due to their sizable wings and extra actuators as manifested in Fig. 3. Their power loading is below 7 g/W despite their relatively high masses. To address this, (iv) revolving-wing multi-modal aerial robots have been proposed [15], [16], [25]. These innovative designs utilize high-speed body rotation and oppositely placed wings for lift generation during hovering for enhanced flight efficiency. Transition to forward flight is achieved through active morphing mechanisms that reconfigure wing and propeller orientations. The revolving-wing concept offers potential efficiency gains in both flight modes [26]. However, these designs necessitate extra servo motors for flight control and reconfiguration, introducing structural complexity and additional mass, rendering them less than ideal for small aerial vehicles. Notably, all multimodal MAVs in Fig. 3 remain over 250 g, placing them beyond the threshold for unlicensed flight in most jurisdictions. Our work directly addresses this challenge by introducing a novel bimodal aerial robot that achieves mode transformation through passive mechanisms, eliminating the need for additional actuators and thereby reducing structural complexity and weight while retaining flight efficiency in both hovering and forward flight modes with a total mass of only 39 g.

III. Aerodynamically Bistable Design for Bimodal Flight

A. Robot Platform Overview

The proposed aerial robot possesses three separate aerodynamic surfaces: a pair of flat wings and a flat tail as illustrated in Fig. 1A and B. In between, a flight control board (Bitcraze Crazyflie 2.1) is incorporated with the structural component as the central fuselage, resulting in a total mass of 38.8 g. In the forward flight mode (shown in Fig. 1A and Fig. 4), the robot adopts a conventional swept-back configuration, similar to our previous aircraft [32]. The two flat wings are mounted to the main body via two elastic joints, allowing the wings to sweep backward and forward by up to $\pm 15.5°$ as constrained by physical joint stoppers as demonstrated in Supplementary Movie 1. Two motor-driven propellers are mounted at the spanwise center of the wings. The tail, notably smaller than the wings, is rigidly affixed as a horizontal stabilizer. This configuration constitutes an airplane with a passive variable-sweep mechanism and longitudinal flight stability. The pitch and the forward flight path angle of the robot are dynamically coupled but can be regulated by varying the net thrust of the two propellers as detailed in [32]. Similar to our previous design, this robot lacks a vertical stabilizer. Instead, it relies on active yaw control achieved through differential thrusts of the two propellers.

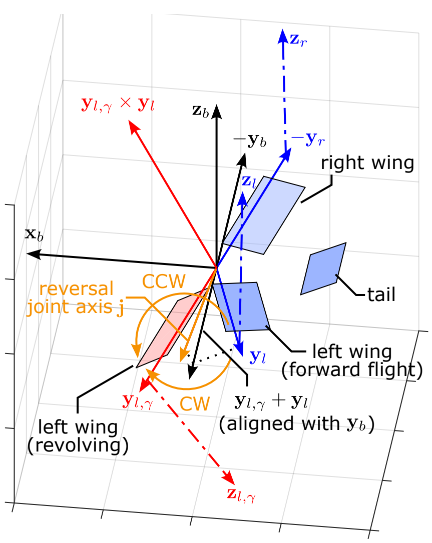

Fig. 4. A Schematic diagrams showing the geometry of the robot in forward flight mode. The figure illustrates the definitions of the wing swept and the dihedral angles.

To enable a transformation to the second flight mode, another passive revolute joint is incorporated between the left wing and the fuselage, permitting the wing to flip and reverse over along an axis almost parallel to the wing's leading edge. The rotational axis of this joint, as well as the joint limits (realized by joint stoppers) is specifically designed for the two modes of operations. In the forward flight mode, the reversible wing rests at the top stopper as shown in Fig. 1A and C. By reversing the wing, the robot transforms into the revolving (or hovering) mode and the left wing is in contact with the bottom stopper as shown in Fig. 1B and D and Supplementary Movie 2. In this mode, the propellers and the wings are directed in the opposite directions. Neglecting the aerodynamic force generated by the small tail while revolving, the robot is functionally and morphologically similar to the previous samara-inspired revolving-wing robot [26], [29], exhibiting efficient hovering.

The robot is designed to passively retain its assumed configuration in both flight modes without the need for extra actuators or latch mechanisms. This is accomplished through an aerodynamically bistable design, where the reversible wing's configuration is sustained by aerodynamic forces. To achieve this aerodynamic bistability and ensure flight stability in both modes, the wing configuration and the reversal joint must adhere to specific criteria, which are detailed below.

B. Wing Configuration in Forward Flight Mode

In the forward flight mode, stability conditions for fixed-wing MAVs must be considered. We design the wings to be back-swept with positive dihedral angle for roll stability. Additionally, a fixed horizontal stabilizer with a negative pitch is incorporated at the rear section to provide longitudinal restoring torque in flight. This configuration, when combined with an active yaw controller, allows the robot to be passively stable in both longitudinal (pitch) and lateral (roll) [32], [54].

To define the wing configuration, the body frame, associated with the rotation matrix $\mathbf{R}_b = [\mathbf{x}_b, \mathbf{y}_b, \mathbf{z}_b]$, is established at the center of mass (CoM) of the airframe, with $\mathbf{x}_b = [1, 0, 0]$ pointing forward and $\mathbf{z}_b = [0, 0, 1]$ pointing upward as shown in Fig. 4. This allows the orientation of the aerodynamic surfaces and the joints to be specified with respect to $\mathbf{R}_b$. In forward flight, the wings are characterized by (i) a sweep angle θ and (ii) a constant dihedral angle of ψ, both depicted in Fig. 4. We introduce the wing-attached frames. For simplicity, we assume the configuration of both wings remain symmetrical, such that the orientation of the right and left wings can be respectively described by the following rotation matrices :

$$\mathbf{R}_r(\theta) = \begin{bmatrix} \mathbf{x}_r & \mathbf{y}_r & \mathbf{z}_r \end{bmatrix} = \mathbf{R}_x\left(-\frac{\psi}{2}\right)\mathbf{R}_z(\theta)\,\mathbf{R}_b,$$
$$\mathbf{R}_l(\theta) = \begin{bmatrix} \mathbf{x}_l & \mathbf{y}_l & \mathbf{z}_l \end{bmatrix} = \mathbf{R}_x\left(\frac{\psi}{2}\right)\mathbf{R}_z(-\theta)\,\mathbf{R}_b, \quad (1)$$

where $\mathbf{R}_x(\cdot)$ and $\mathbf{R}_z(\cdot)$ denote rotation matrices about x and z axes. As seen in Fig. 4, vectors $\mathbf{z}_r$ and $\mathbf{z}_l$ are always orthogonal to the wing surfaces. The sweep angle describes the rotation of the wing about $\mathbf{z}_r$ and $-\mathbf{z}_l$, measured with respect to $\mathbf{y}_b\mathbf{z}_b$ plane. By default, the wing rests at the most back-swept position $\theta = \theta_-$, due to the restoring torque from the elastic component. Due to the elastic joints, the wings are swept back at $\theta = \theta_-$ by default. Increasing the propelling thrust creates torque about the joint, sweeping the wing forward (with the maximum limit of θ_+ as determined by the joint stopper). This change in the center of pressure with respect to the center of mass affects the pitch dynamics, allowing the longitudinal flight dynamics to be controlled as detailed in [32]. Vectors $-\mathbf{y}_r$ and $\mathbf{y}_l$, denoting the spanwise directions of the right and left wings pointing from root to tip, are functions of θ. Equation 1 means the surfaces of the wings ($\mathbf{x}_r - \mathbf{y}_r$ and $\mathbf{x}_l - \mathbf{y}_l$ plane) and the frontal vector $\mathbf{x}_b$ are coplanar, such that $\mathbf{z}_r$ and $\mathbf{z}_l$ are orthogonal to $\mathbf{x}_b$ and independent of the wing sweep angle θ

C. Revolving Mode and Wing Reversal Joint

Unlike the forward flight, in which the wings are nominally symmetric about the sagittal plane ($\mathbf{x}_b\mathbf{z}_b$) as illustrated in Fig. 5, the revolving flight requires the wings to have 2-fold rotational symmetry about the revolving axis. To transform the robot from forward to revolving flight, we leverage the reversal joint to flip the left wing backward. This rotates the entire left wing and its propeller about the wing reversal joint axis $\mathbf{j}$ by an angle γ, as dictated by the stopper. The orientation of the left wing in this configuration is given by

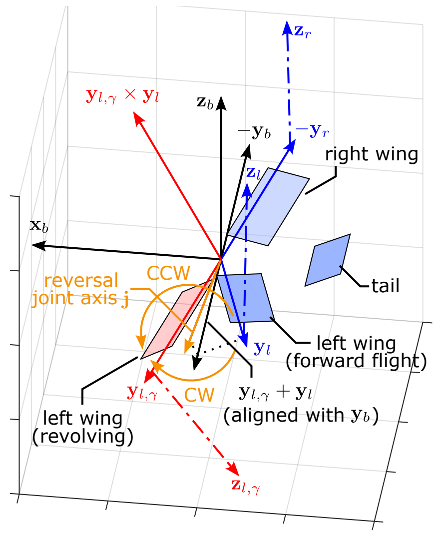

Fig. 5. An isometric drawing depicting the vectors relevant to the wing configurations in both forward and revolving flight modes.

$$\mathbf{R}_{l,\gamma} = \mathbf{R}_j(\gamma)\mathbf{R}_l(\theta) = \begin{bmatrix} \mathbf{x}_{l,\gamma} & \mathbf{y}_{l,\gamma} & \mathbf{z}_{l,\gamma} \end{bmatrix}, \quad (2)$$

where $\mathbf{R}_j = \mathrm{rot}(\mathbf{j}, \gamma)$ denotes a rotation matrix about an axis $\mathbf{j}$ by an angle γ. While revolving, we restrict the propelling thrusts to ensure the wings settle at their default sweep ($\theta = \theta_-$), maintaining structural symmetry. In the design process, the desired wing configuration $\mathbf{R}_{l,\gamma}$ is first chosen, and the required joint axis $\mathbf{j}$ and angle γ are determined by solving for $\mathbf{j}$ and γ that are compatible with $\mathbf{R}_j(\gamma)$ from $\mathbf{R}_j(\gamma) = \mathbf{R}_{l,\gamma}\mathbf{R}_l^{\mathrm{T}}(\theta)$.

As the two wings should be arranged with 2-fold rotational symmetry in the revolving mode, this implies the spanwise vector of both wings must be aligned or $\mathbf{y}_r = \mathbf{y}_{l,\gamma}$ as shown in Fig. 5. This requires $\mathbf{j}$ to lie on a plane that is coplanar with vectors $\mathbf{y}_{l,\gamma} + \mathbf{y}_l$ and $\mathbf{y}_{l,\gamma} \times \mathbf{y}_l$ as displayed in Fig. 5, imposing a condition

$$\mathbf{j} = \mathbf{y}_{l,\gamma} + \mathbf{y}_l + c\left(\mathbf{y}_{l,\gamma} \times \mathbf{y}_l\right), \quad (3)$$

for a tuning parameter c. Notice that the vector $\mathbf{y}_{l,\gamma} + \mathbf{y}_l = -\mathbf{y}_r + \mathbf{y}_l$ aligns with $\mathbf{y}_b$ because of the symmetric nature of the two wings. Meanwhile, $\mathbf{y}_{l,\gamma} \times \mathbf{y}_l$ represents the rotational symmetry axis in revolving wing mode, coinciding with the revolving axis of the robot as illustrated in Fig. 5.

Another critical constraint for the design is the pitch angle of the wings in the revolving mode, predefined to be $\beta_w = 19°$, based on our previous findings [26]. This angle can be written as

$$\beta_w = \frac{1}{2}\arccos\left(-\mathbf{z}_r^{\mathrm{T}} \cdot \mathbf{z}_{l,\gamma}\right). \quad (4)$$

Combining Eq. 3 and Eq. 4, we can numerically solve for $\mathbf{j}$, γ and c. With the given design parameters listed in Table I, there exist two solutions corresponding to the same rotation ($\mathbf{j} = [0.05, 0.96, 0.09]^{\mathrm{T}}$) but in clockwise and counterclockwise directions ($\gamma = -142°, 218°$) as presented in Fig. 5. Only one direction, clockwise ($\gamma = -142°$), is chosen to assure the structure is aerodynamically bistable as detailed below.

TABLE I
PARAMETERS FOR THE DESIGNED MODEL AND FABRICATION.

Para.	Description	Value	Unit
θ_-	default backswept angle	-15.5	deg
θ_+	maximum forward sweep	15.5	deg
ψ	dihedral angle of the wings	16	deg
β_w	wing pitch angle in revolving mode	19	deg
β_t	tail pitch angle	30	deg
S_w	area of the a single wing	25×6.5	cm^2
S_t	area of the tail	11×4.2	cm^2
m	mass of the robot	38.8	g
I_z	yaw moment of inertia	580	kg·mm^2
I_y	pitch moment of inertia	24	kg·mm^2
l_t	distance of tail from CoM	10.3	cm
l_{span}	distance from the of the left wing to the reversal joint	15	cm

D. Design for Aerodynamic Bistability

Despite the fact that the wing reversal joint is designed to be free-to-rotate, aerodynamic loads exerted on the wings in both forward and revolving modes should nominally inhibit rotation or transformation. This maintains the wings in their current configuration without the need for a latch mechanism or actuator. This bistability simplifies the structure and eliminates the need for additional actuators.

The robot's flat wings allow us to model its aerodynamics using flat plate theory [32], effectively capturing the dominant aerodynamic characteristics needed for modeling and control [26], [29], [32], [55]. The theory assumes lift and drag coefficients of

$$C_L = 2\sin(\alpha)\cos(\alpha) \quad \text{and} \quad C_D = 2\sin^2(\alpha),$$

where the resultant aerodynamics forces f_A (a vector sum of lift and drag) are always perpendicular to the wing surface, regardless of the angle of attack α [32],

$$f_A \mathbf{z}_{l,r} = \rho S_w \sin(\alpha) \|\mathbf{U}\|^2 \mathbf{z}_{l,r}, \tag{5}$$

in which ρ is the air density, S_w is the wing area, $\mathbf{U}$ is the relative velocity, and $\mathbf{z}_{l,r}$ is an upward-pointing vector normal to the wing surface. Additionally, we assume the centers of pressure (CoP) of the wings are located at their spanwise centers and at the quarter-chord point from the leading edge [56] as illustrated in Fig. 4.

To realize aerodynamic bistability, the torque induced by aerodynamic pressure on the wing reversal joint must oppose the feasible rotation direction in each mode. In forward flight, the torque attributed to the aerodynamic load on the wing reversal joint $\mathbf{j}$, after the projection onto the joint axis is

$$\tau_r = -\mathbf{j} \cdot (f_A \mathbf{z}_l \times l_{span} \mathbf{y}_l), \tag{6}$$

where l_{span} is the spanwise length from the CoP to the reversal joint as shown in Fig. 4. The spanwise vector $\mathbf{y}_l$ varies with the wing sweep angle θ, affecting the joint torque τ_r (whereas $\mathbf{z}_l$ is independent of θ). For the proposed robot with parameters listed in Table I, during forward flight ($f_A > 0$), τ_f is positive when $\theta < 2.7°$ and is negative when $\theta > 2.7°$. Consequently, to render the wing configuration stable in forward flight mode at low and negative sweep angle, we design the wing reversal joint limits to allow only a negative (clockwise) rotation as shown in Fig.5. This only permits a wing rotation in the $-\mathbf{j}$ direction, preventing the wing rotation when $\theta < 2.7°$. That is, in forward flight, the wing configuration remains stable as long as θ is lower than 2.7°.

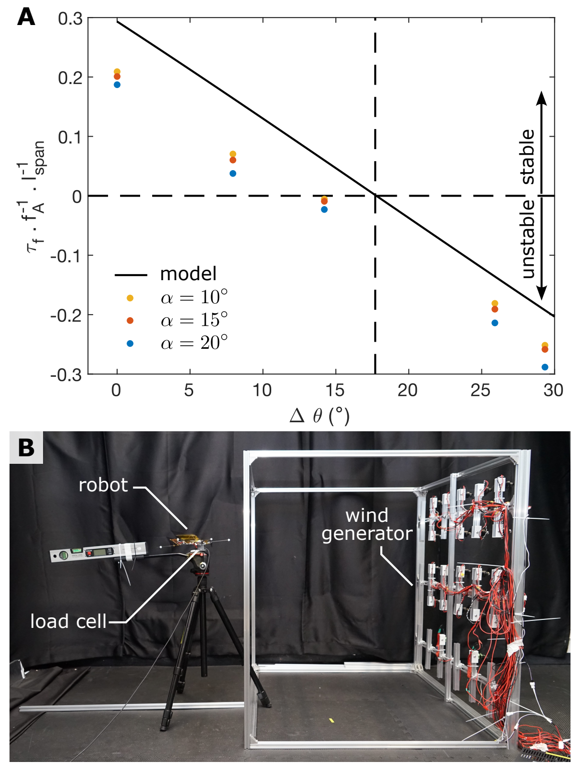

Fig. 6. (A) Aerodynamic torque (normalized) applied on the reversal joint with respect to the sweep angle of the wing. The plots show measurement results and the model prediction. (B) Experimental setup for aerodynamic force and torque measurements, including a custom-made wind generator.

In contrast, in the revolving mode, the left wing is reverse with $\gamma = -199°$. The torque on the joint is given by

$$\tau_r = \mathbf{j} \cdot (f_A \mathbf{z}_{l,\gamma} \times l_{span} \mathbf{y}_{l,\gamma}), \tag{7}$$

as the aerodynamic force aligns with $-\mathbf{z}_{l,\gamma}$. Notably, τ_r is negative for $\theta_- < \theta < 2.7°$. By design of the stoppers, rotation in the respective direction is not permitted in revolving mode. Therefore, the structural stability condition for revolving flight is also $\theta < 2.7°$.

To sum up, with the proposed wing configuration and wing reversal joint stoppers, the aerodynamic bistability is attained as long as the wing sweep angle is below 2.7° as shown in Fig. 5. This condition is warranted at low thrust commands. This aerodynamically bistable design allows the robot to maintain its flight configuration autonomously, eliminating the need for additional actuators or latch mechanisms. Additionally, the mode transformation can be accomplished by either increasing the propelling thrust or altering the direction of the aerodynamic force. Both can effectively change the direction of τ_r in Eq. 6 and Eq. 7, rendering it possible to accomplish the wing reversal on demand during flight.

IV. Strategy for Flight Mode Transformation

A. Forward to Revolving Fight

As described above, the torque on the wing reversal joint depends on the location of the CoP of the wing as governed by the sweep angle θ. The sweep angle can be manipulated through propelling thrust. To remain in the forward flight mode , θ should be lower than the critical angle of 2.7°. Varying the CoP within this range still allows the pitch motion and longitudinal dynamics of the robot to be controlled. On the contrary, breaking this limit destabilizes the structural aerodynamic stability, inducing the transformation from forward to revolving flight mode.

To initiate the transformation from forward to revolving flight, the CoP is shifted forward by increasing throttle on both propellers simultaneously. This maneuver initially causes the entire robot to pitch up as long as θ remains below 2.7°. Once θ exceeds this threshold, τ_r becomes negative, triggering the left wing to rotate. This mode transformation is accomplished without employing any extra actuators.

B. Revolving to Forward Flight

The transformation from revolving to forward flight is initiated by powering off the propulsion system while the robot is in revolving mode. This process leverages the relatively large pitch angle of the wings during revolving flight ($\beta_w = 19°$) to generate significant aerodynamic drag torque, which quickly decelerates the robot's rotation once the thrust disappears. As the revolving speed decreases, lift is substantially reduced, causing the robot to stall and begin descending. We model this deceleration process, neglecting lateral motion. The aerodynamic forces acting on the robot arise from the yaw motion and the vertical velocity induced by gravity. A simulation, detailed in the Supplementary Material, shows that reducing the revolving speed from 20 rad/s to 0 rad/s takes 0.53 s, during which the robot descends by 0.6 meters.

Once the yaw motion stops, the transition progresses to pitch rotation and longitudinal movement. Continuing the descent, the drag generated by the tail shifts the center of pressure (CoP) rearward relative to the center of mass (CoM), inducing a pitch-down moment. This torque causes the robot's nose ($\mathbf{x}_b$) to point downward, aligning the relative airflow with the $-\mathbf{x}_b$ direction mainly contributed from tail as:

$$\tau_{tail} = \frac{l_t}{\cos\beta_t}\rho S_t \sin(\alpha)\left\|\mathbf{U}\right\|^2, \tag{8}$$

where l_t is the tail CoP's projected distance from the CoM along $\mathbf{x}_b$,S_t is the tail area, and β_t is the tail pitch angle relative to the body. The AoA α, defined in Eq. 5, depends on the instantaneous air velocity $\mathbf{U}$.

As the robot's vertical speed increases and its nose pitches downward, the relative airflow begins to affect the wings. Specifically, the left wing generates an aerodynamic force in the $\mathbf{z}_{l,\gamma}$ direction, which is opposite the force it generates during revolving flight. When the relative inflow aligns to the left wing's local frame with an angle less than 90° ($-\mathbf{U}_v \cdot \mathbf{z}_{l,\gamma} > 0$), the aerodynamic forces destabilize the left wing, causing it to reverse into the forward flight configuration. This reversal process is governed by the torque defined in Eq. 7. At this stage, the robot transitions into forward flight mode, with the wings stabilizing into their fixed-wing configuration due to aerodynamic forces.

A simulation, detailed in Supplementary Materials, confirms this transition, showing that the robot reaches its lowest altitude after an 8.1-m descent before gradually climbing to achieve level flight. With the initial 0.6-m descent, the total altitude loss in the simulation is 8.7 m.

V. Experimental Validations

A. Validation of Aerodynamic Bistability

To verify the principle and feasibility of the aerodynamic bistability, we conducted an static experiment to simulate forward flight situations. The structural stability was evaluated by measuring the aerodynamic force and torque. As shown in Fig. 6B, we employed 20 brushless motors (2204 2300kv) with 5-inch propellers to generate airflow covering an area of 0.8 m × 0.8 m. This dense arrangement of small propellers generate turbulence flow, devoid of rotational wake produced by a single large propeller. The robot was affixed on a 6-axis load cell (ATI nano 25), mounted on a tripod, and placed 1.3 m in front of the wind generator. The load cell was located close to and beneath the CoM of the robot, allowing us to directly measure the total aerodynamic torque and lift generated by the two wings and tail.

We recorded the torque and force when the robot was equipped with and without wings. Considering the fact that the wing reverseal joint axis $\mathbf{j}$ is almost parallel to $\mathbf{y}_b$ (see Fig. 5), we take half of the total pitch torque (measured about $-\mathbf{y}_b$) and the upward force ($\mathbf{z}_b$ direction) after subtracting out the torque and force generated by the tail to approximately represent τ_r and f_a from one wing. For the airspeed of approximately 4.8 m/s (measured by an anemometer, Kanomax 6036), we measured τ_r and f_a over various the body pitch angles α (equivalent to angle of attack): 10°, 15° and 20°, and at different wing sweep angles θ: -15.5°, -7.6°, -1.3°, 10.4° and 13.8°. Each measurement was taken as an average over 20 s. This leads to the total of 15 datapoints as shown in Fig. 6A. The torque τ_r in 6, after normalized by the aerodynamic force from 5, is independent of α. Hence, all measurements produce similar trends to the model predictions, approximately independent of α as anticipated. However, there exists a consistent offset which indicates a misalignment in the wing sweep angle θ of approximately 3.5°. This is likely because of the different between the actual and modeled locations of the CoP. Overall, the outcomes verify that the normalized torque is positive and the structure of the airframe is aerodynamically stable when θ is lower than $-0.8°$ (versus 2.7° predicted by the model), for the tested range of the AoA.

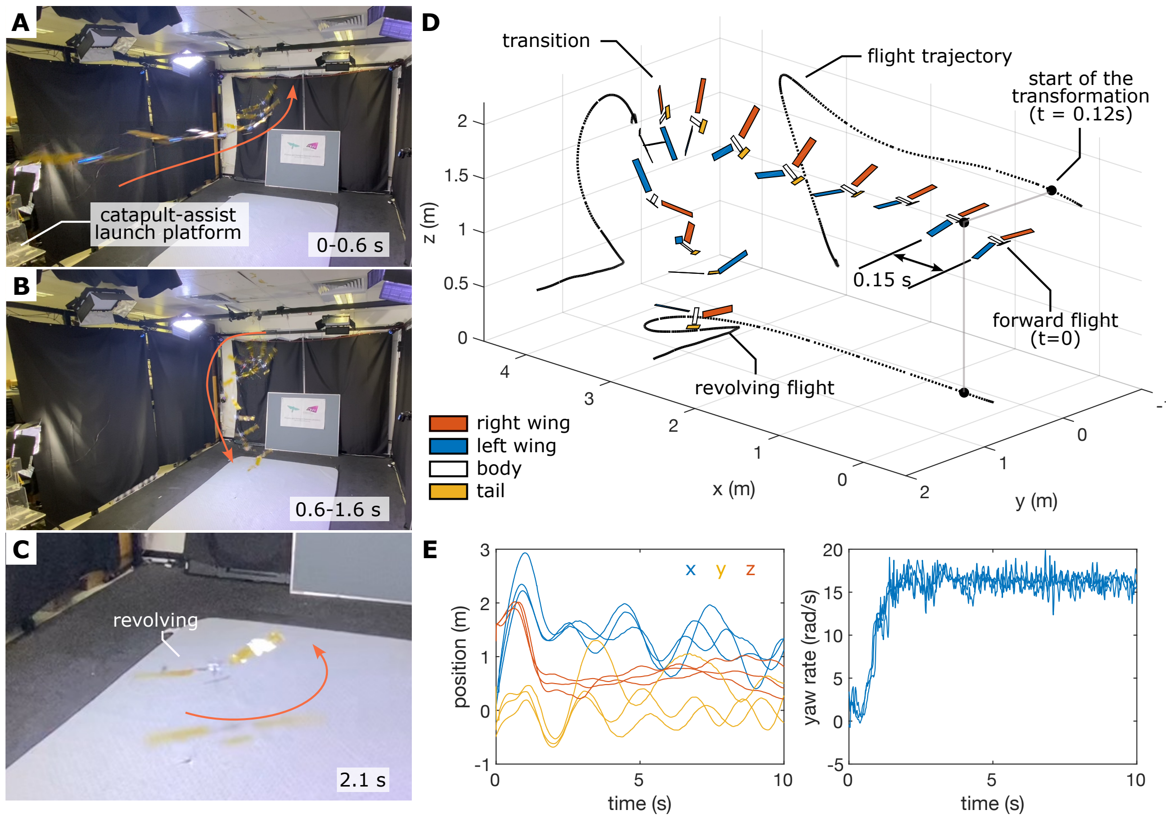

Fig. 7. Demonstration of transformation from forward to revolving flight. (A), (B) and (C) Sequence of composite images capturing the transformation process. (D) The flight trajectory and configurations of the wings in the transformation process. The data are presented with time intervals of 0.15 s, except for the last interval, which is 0.95 s. (E) Position and yaw rate of the robot in three repeated transformation experiments.

B. Forward Flight Demonstration

To validate the robot's forward flight capabilities, we conducted three separate tests in open spaces, ranging from 20 to 40 m in distance, as shown in Supplementary Movie 1.

For each test, the robot was hand-launched to initiate takeoff. The initial speed provided during the throw caused the robot to climb slightly before its thrust and heading control systems engaged, allowing it to transition smoothly into straight, level flight. The tail design provided passive longitudinal stability, enabling the robot to maintain a relatively consistent speed and angle of attack (AoA). During equilibrium flight (1 s after launch), the robot demonstrated a cruising speed of about 5.2±0.7 m/s, maintaining a stable and nearly horizontal flight path with pitch angle variations limited to 0±2°. The average pitch angle of the body and the wings' AoA were approximately 18°. Yaw angular velocity data collected during these flights are provided in Fig. S8.

These tests effectively demonstrate the robot's ability to achieve stable, controlled forward flight in outdoor conditions, validating its design for efficient cruising capabilities.

C. Revolving Flight Demonstration

To evaluate the performance of the robot's revolving flight, we conducted outdoor experiments focusing on hovering and slow horizontal flights, even in the presence of wind.

The robot's ability to hover stably was tested in mild wind conditions as shown in Supplementary Movie 3, with instantaneous wind speeds ranging between 0.6 m/s and 2 m/s (measured using an anemometer, Kanomax 6036). In the open-loop hovering flight, the robot's attitude was passive stabilized by aerodynamic effects. During three trials lasting 40–60 seconds each, the robot maintained stable hovering with minimal horizontal drift. The total horizontal displacement between takeoff and landing was approximately 2 m, despite some wind flow. Data on the revolving rate recorded during these experiments are shown in Fig. S6.

Additionally, the robot's performance in slow translation was tested as shown in Fig. 8 B. Using the control algorithm described in [26] with yaw feedback provided by an onboard IMU, a human operator commanded the robot to perform back-and-forth flight, resulting in a total travel distance of approximately 20 m (10 m forward and 10 m back), with an average translational speed of 0.25 m/s. The round trip took 39 s shown in Supplementary Movie 4. The yaw feedback data recorded during this flight is presented in Fig. S7.

These tests effectively demonstrate the robot's ability to maintain passive stable hovering flight in variable wind conditions and perform controlled horizontal translations, underlining the robustness and versatility of the revolving flight mode in outdoor settings.

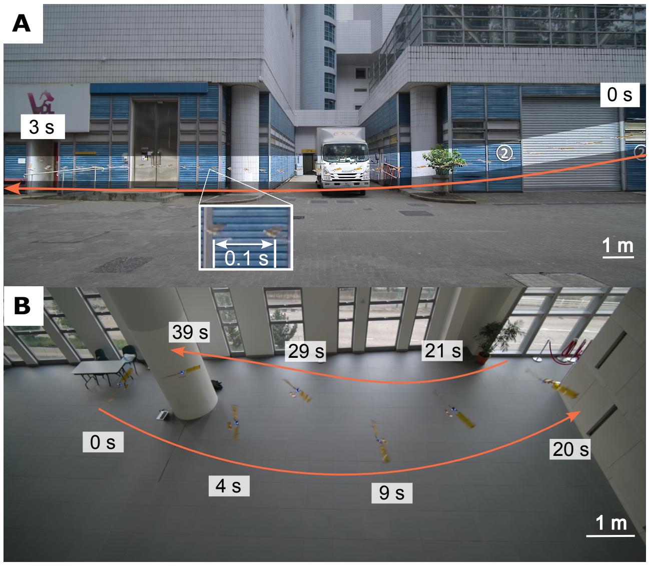

Fig. 8. (A) Forward level flight with constant thrust over 20 m. After a hand-assisted launch, the robot initially descended for 1 s before gradually stabilizing into equilibrium level flight. Frames shown at 0.1-s intervals. In equilibrium, the robot maintained approximately 18° AoA with a flight path of 0° ± 2° and a cruising speed of 5.2±0.7 m/s. (B) Controlled revolving flight convering over 20 m distance in total (10 m forward and 10 m back).

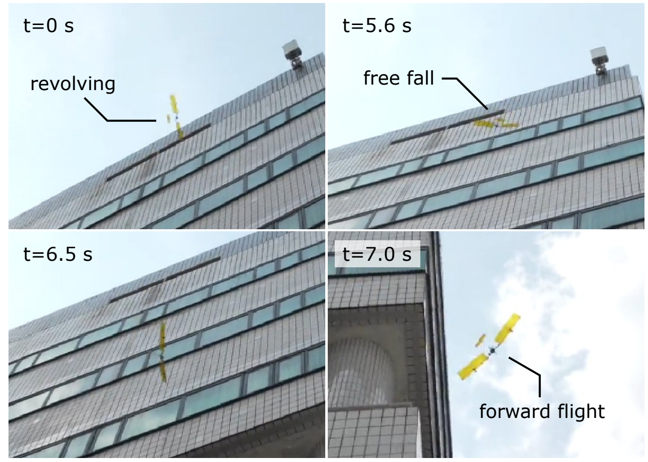

Fig. 9. Sequence of experimental images demonstrating transformation from revolving to forward flight (refer to Supplementary Movie 6).

D. Demonstration of Midair Transformation from Forward to Revolving Flight

We conducted indoor experiments to evaluate and demonstrate the transformation from forward to revolving flight shown in Supplementary Movie 5. These experiments took place in a 7 m × 3 m × 2.5 m indoor arena equipped with ten motion capture cameras (OptiTrack Prime 13w), covering a space of 5m × 3m × 2.5m. The motion capture system measures the position and orientation of the robot's body, left wing, and right wing separately. To achieve stable flight, the robot was programmed to actively stabilize yaw using differential thrust and the onboard gyroscope feedback [32]. All commands and communications implemented on the ground station computer using Python, operating at a frequency of 100 Hz via radio communication (Bitcraze Crazyradio PA) and the Crazyflie Python API.

Space constraints of the indoor environment prevented long forward flights. Hence, we employed a catapult-assisted launch platform to rapidly accelerate the robot to its cruising speed [32]. Immediately after launched, the robot flew with a backswept configuration, indicating a regular forward flight mode as captured in Fig. 7 A and D. Once the robot entered the region covered by the motion capture system and traveled beyond 1 m, we initiated the mode conversion by increasing propelling thrust. As thrust increased, both wings swept forward, simultaneously causing a noticeable climbing motion (Fig. 7 A and D). After the wings swept forward, the displaced CoP caused the left wing to reverse. The wing rotation took approximately 0.9 s, during which the the robot experienced flight instability, losing its altitude by approximately 1.2 m. After this transformation, the change in the thrust direction of the left wing induced the robot start to revolve, generating lift and halted the altitude loss. The robot then hovered at an altitude of 0.25 m (Fig. 7B, C and D). In the revolving mode, the robot yaw rate reached approximately 16 rad/s. The entire transformation took approximately 1.65 s.

We conducted three repeated transformation experiments as shown in Supplementary Movie 5. The recorded position and yaw rate are shown in Fig. 7 E. The robot performed similarly in all experiments, implying the reliability and repeatability of the developed strategy.

E. Demonstration of Midair Transformation from Revolving to Forward Flight

The transition from revolving to forward flight was demonstrated in outdoor experiments, with the robot starting from an altitude of 15–20 m. The transformation was initiated by remotely disabling the propulsion system while the robot was revolving. As predicted by our model and the simulation, the robot experienced rapid yaw deceleration within 0.5 s of thrust termination, followed by a brief stall and a descent of approximately 1.4 m (estimated from the video according to the procedure described in Supplementary Materials and Fig. S5). During this, the robot's body remained pitched upward, with the tail hanging lower than the body and wings. The observed drop altitude during this rotational deceleration period was about 0.8 meters greater than the simulated value (refer to Supplementary Materials). The discrepancy is likely attributed to the assumptions used in the video analysis and simplifications in our model, which assumes the robot maintains a perfectly upright orientation. In reality, angular deviations from vertical during transition alter the effective lift and drag profiles, potentially influencing the deceleration dynamics and the resulting drop altitude.

The subsequent pitch-down moment, induced by tail drag, oriented the robot into a nose-down attitude. This orientation change, combined with the increasing downward velocity, created the necessary conditions for wing reversal. In our experiments, it took less than 1 s for the left wing to reverse due to the instantaneous change in aerodynamic loading. After wing reversal, we adjusted the thrust to an appropriate level to achieve steady, level flight. The robot gradually transitioned to stable forward flight over approximately 6.5 seconds, as shown in Fig. 9. During this process, we estimate that the robot experienced an additional descent of approximately 5 m (Fig. S5). The transition took 2-3 s from the moment the revolving motion stopped. The actual altitude loss was lower than prediction and the simulation (see Supplementary Materials). This discrepancy may be attributed to the possibility that the total drag of the robot might be higher than our estimates based solely on tail and wing surfaces.

We successfully replicated this transition in multiple trials, with three examples provided in Supplementary Movie 6. These demonstrations validate our model of the transition process and highlight the effectiveness of our passive wing-reversal mechanism in achieving multimodal flight. It's worth noting that while this transition method proves effective in open spaces, it requires an altitude loss of approximately 6.4 m during the transformation process. This characteristic may limit its applicability in cluttered environments.

F. Power Expenditure and Endurance

With only two actuators, the robot is capable of operating in two flight modes via passive morphing mechanisms. This reduced actuator requirement lowers redundant mass, enhancing flight efficiency. To evaluate power consumption, we conducted endurance flight tests. We measured power consumption in both modes by recording the battery voltage and motor Pulse-Width Modulation duty ratio during flight and replicated these conditions in an offline benchtop setup. Employing a current sensor (HW-872A) and a data acquisition system (National Instrument, PCI-6259), the voltage and current were sampled at 1000 Hz.

In the revolving mode, the robot achieved a maximum hovering time of 478 s (Supplementary Movie 7). The benchtop test measured its average power consumption of 6.67 W, yielding a power loading of 7.11 g/W (Fig. S9).

For forward flight, site constraints prevented continuous long-range assessments. Instead, we measured power in equilibrium cruising flight. By adjusting motor voltage to maintain a 0° flight path angle across three trials (20-40 m distances), we measured average power in forward flight at 4.63 W, or 10.24 g/W power loading (Fig. S9).

Compared to lightweight rotorcraft (<100 g), our 47.4-g robot demonstrates superior efficiency due to its larger aerodynamic surfaces [26]. In contrast, multimodal aerial robots typically weigh 0.3–10 kg (Fig. 3). Our robot's compact multimodal flight capability stems from its passive morphing structure, eliminating actuators for morphing. While larger multimodal drones achieve more efficient flight due to higher Reynolds numbers and better lift-to-drag ratios [26]. their hover power loading is not significantly better than our robot's due to compact rotor usage and actuator redundancy. Some tailless multimodal drones cannot maintain low angles of attack in forward flight, resulting in power loadings similar to or lower than both their hover mode and our robot. Only large, tailed multimodal vehicles with more actuators (4-11) and complex structures surpass our robot's efficiency, though their complexity makes miniaturization challenging (Table S1). Our drone effectively balances efficiency and structural complexity at miniature scale, demonstrating significant advantages over other multimodal aerial robots.

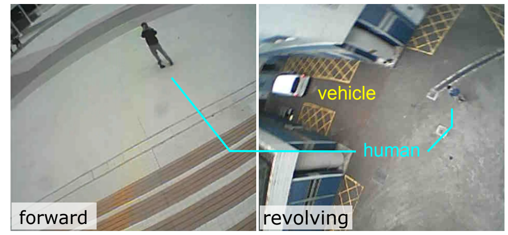

Fig. 10. Image frames taken from an the onboard camera in both forward and revolving flight modes.

G. Demonstration of Aerial Monitoring

To showcase potential applications, we mounted a 3.6-g camera (MingChuan 701U) on the robot's frame (Fig. S10). During outdoor flights, the robot successfully captured still images and videos in both flight modes, providing aerial views from various altitudes (Fig. 10 and Supplementary Movie 1). The captured imagery clearly identified objects such as people, buildings, and vehicles, even during rotation and forward flight, confirming its capability for both stationary and dynamic monitoring. Additionally, the camera accounted for 9% of the robot's total weight, highlighting its ability to carry moderate payloads while maintaining flight performance.

VI. Conclusions

In this work, we have presented the design and implementation of a multimodal MAV capable of passively transitioning between forward flight and revolving hover modes. By employing passive revolute joints and an aerodynamically bistable structure, the MAV achieves two distinct flight modes without the need for additional actuators or complex locking mechanisms. The bistable configuration allows the reversal joint to maintain its position under aerodynamic forces during each flight mode, enabling a robust and efficient mode transition.

The passive variable-sweep mechanism plays a crucial role in this design by leveraging the principles of aerodynamic bistability. By adjusting the CoP of the wings relative to the CoM, the MAV can transition from forward flight to revolving mode through a controlled increase in propeller thrust. This aerodynamic stability ensures that the vehicle naturally converges to the revolving mode under passive dynamics. Conversely, the transition from revolving to forward flight is achieved by simply disabling the propellers at a high altitude. As the vehicle decelerates and enters free fall, the aerodynamic forces restore the MAV to its forward flight configuration. However, the current open-loop revolving-to-forward-flight transformation strategy cannot regulate or control the forward flight direction of the vehicle immediately after the transformation, owing to the fast yaw rotation of the robot prior to the transformation. This somewhat restricts its applicability, especially in narrow or cluttered environments. Future work will focus on developing transformation methods that are more compatible with such challenging scenarios.

While simplified aerodynamic models proved sufficient for producing the bistable mechanism and enabling a functional design, future work could incorporate Computational Fluid Dynamics (CFD) simulations to refine the aerodynamic efficiency further. CFD could provide deeper insights into flow interactions during transitions and help optimize the wing geometry for improved stability and performance.

Despite these limitation, the structural efficiency and aerodynamic design of the robot offer the potential for efficient flight in both modes, expanding the operational envelope of small-scale aerial robots. The efficient locomotion bring potential for real-world applications, including prolonged surveillance, monitoring or mapping. The lightweight and efficient design of the robot, equipped with only two propellers as actuators, demonstrates a promising approach to achieving versatile flight capabilities without the introduction of redundant actuators or complex morphing mechanisms.

References

[1] X. Zhou, X. Wen, Z. Wang, Y. Gao, H. Li, Q. Wang, T. Yang, H. Lu, Y. Cao, C. Xu *et al.*, "Swarm of micro flying robots in the wild," *Science Robotics*, vol. 7, no. 66, p. eabm5954, 2022.

[2] H. Jia, S. Bai, R. Ding, J. Shu, Y. Deng, B. L. Khoo, and P. Chirarattananon, "A quadrotor with a passively reconfigurable airframe for hybrid terrestrial locomotion," *IEEE/ASME Transactions on Mechatronics*, vol. 27, no. 6, pp. 4741–4751, 2022.

[3] N. Chen, F. Kong, W. Xu, Y. Cai, H. Li, D. He, Y. Qin, and F. Zhang, "A self-rotating, single-actuated uav with extended sensor field of view for autonomous navigation," *Science Robotics*, vol. 8, no. 76, p. eade4538, 2023.

[4] P. H. Nguyen, K. Patnaik, S. Mishra, P. Polygerinos, and W. Zhang, "A soft-bodied aerial robot for collision resilience and contact-reactive perching," *Soft Robotics*, vol. 10, no. 4, pp. 838–851, 2023.

[5] M. Hassanalian and A. Abdelkefi, "Classifications, applications, and design challenges of drones: A review," *Progress in Aerospace sciences*, vol. 91, pp. 99–131, 2017.

[6] D. Sufiyan, L. S. T. Win, S. K. H. Win, Y. H. Pheh, G. S. Soh, and S. Foong, "An efficient multimodal nature-inspired unmanned aerial vehicle capable of agile maneuvers," *Advanced Intelligent Systems*, vol. 5, no. 1, p. 2200242, 2023.

[7] M. Di Luca, S. Mintchev, Y. Su, E. Shaw, and K. Breuer, "A bioinspired separated flow wing provides turbulence resilience and aerodynamic efficiency for miniature drones," *Science Robotics*, vol. 5, no. 38, p. eaay8533, 2020.

[8] R. Bapst, R. Ritz, L. Meier, and M. Pollefeys, "Design and implementation of an unmanned tail-sitter," in *2015 IEEE/RSJ international conference on intelligent robots and systems (IROS)*. IEEE, 2015, pp. 1885–1890.

[9] S. K. H. Win, L. S. T. Win, D. Sufiyan, G. S. Soh, and S. Foong, "An agile samara-inspired single-actuator aerial robot capable of autorotation and diving," *IEEE Transactions on Robotics*, vol. 38, no. 2, pp. 1033–1046, 2021.

[10] H. Jia, S. Bai, and P. Chirarattananon, "Aerial manipulation via modular quadrotors with passively foldable airframes," *IEEE/ASME Transactions on Mechatronics*, vol. 28, no. 4, pp. 1930–1938, 2023.

[11] S. Bai and P. Chirarattananon, "Splitflyer air: A modular quadcopter that disassembles into two bicopters mid-air," *IEEE/ASME Transactions on Mechatronics*, vol. 27, no. 6, pp. 4729–4740, 2022.

[12] H. Bhardwaj, X. Cai, L. S. T. Win, and S. Foong, "Nature-inspired in-flight foldable rotorcraft," *Bioinspiration & Biomimetics*, vol. 18, no. 4, p. 046012, 2023.

[13] X. Cai, S. K. H. Win, H. Bhardwaj, and S. Foong, "Modeling, control and implementation of adaptive reconfigurable rotary wings (arrows)," *IEEE/ASME Transactions on Mechatronics*, vol. 28, no. 4, pp. 2282–2292, 2023.

[14] H. Bhardwaj, X. Cai, S. K. H. Win, and S. Foong, "Design, modeling and control of a two flight mode capable single wing rotorcraft with mid-air transition ability," *IEEE Robotics and Automation Letters*, vol. 7, no. 4, pp. 11 720–11 727, 2022.

[15] J. E. Low, L. T. S. Win, D. S. B. Shaiful, C. H. Tan, G. S. Soh, and S. Foong, "Design and dynamic analysis of a transformable hovering rotorcraft (thor)," in *2017 IEEE International Conference on Robotics and Automation (ICRA)*. IEEE, 2017, pp. 6389–6396.

[16] J. E. Low, L. T. S. Win, J. Le Lee, G. S. Soh, and S. Foong, "Towards a stable three-mode transformable hovering rotorcraft (thor)," in *2018 IEEE/ASME International Conference on Advanced Intelligent Mechatronics (AIM)*. IEEE, 2018, pp. 492–497.

[17] O. Kose, T. Oktay, and E. Özen, "Simultaneous arm morphing quadcopter and autonomous flight system design," *Aircraft Engineering and Aerospace Technology*, vol. 95, no. 10, pp. 1624–1632, 2023.

[18] O. Kose and T. Oktay, "Simultaneous design of morphing hexarotor and autopilot system by using deep neural network and spsa," *Aircraft Engineering and Aerospace Technology*, vol. 95, no. 6, pp. 939–949, 2023.

[19] S. Verling, B. Weibel, M. Boosfeld, K. Alexis, M. Burri, and R. Siegwart, "Full attitude control of a vtol tailsitter uav," in *2016 IEEE international conference on robotics and automation (ICRA)*. IEEE, 2016, pp. 3006–3012.

[20] H. Gu, X. Lyu, Z. Li, S. Shen, and F. Zhang, "Development and experimental verification of a hybrid vertical take-off and landing (vtol) unmanned aerial vehicle (uav)," in *2017 International Conference on Unmanned Aircraft Systems (ICUAS)*. IEEE, 2017, pp. 160–169.

[21] G. Palaia, K. Abu Salem, V. Cipolla, V. Binante, and D. Zanetti, "A conceptual design methodology for e-vtol aircraft for urban air mobility," *Applied Sciences*, vol. 11, no. 22, p. 10815, 2021.

[22] A. Vuruskan, B. Yuksek, U. Ozdemir, A. Yukselen, and G. Inalhan, "Dynamic modeling of a fixed-wing vtol uav," in *2014 international conference on unmanned aircraft systems (ICUAS)*. IEEE, 2014, pp. 483–491.

[23] L. Bauersfeld, L. Spannagl, G. J. Ducard, and C. H. Onder, "Mpc flight control for a tilt-rotor vtol aircraft," *IEEE Transactions on Aerospace and Electronic Systems*, vol. 57, no. 4, pp. 2395–2409, 2021.

[24] X. Lyu, H. Gu, Y. Wang, Z. Li, S. Shen, and F. Zhang, "Design and implementation of a quadrotor tail-sitter vtol uav," in *2017 IEEE international conference on robotics and automation (ICRA)*. IEEE, 2017, pp. 3924–3930.

[25] D. S. B. Shaiful, L. T. S. Win, J. E. Low, S. K. H. Win, G. S. Soh, and S. Foong, "Optimized transition path of a transformable hovering rotorcraft (thor)," in *2018 IEEE/ASME International Conference on Advanced Intelligent Mechatronics (AIM)*. IEEE, 2018, pp. 460–465.

[26] S. Bai, Q. He, and P. Chirarattananon, "A bioinspired revolving-wing drone with passive attitude stability and efficient hovering flight," *Science Robotics*, vol. 7, no. 66, p. eabg5913, 2022.

[27] X. Cai, L. S. T. Win, B. L. Suhadi, H. Bhardwaj, and S. Foong, "A self-rotary aerial robot with passive compliant variable-pitch wings," *IEEE Robotics and Automation Letters*, vol. 8, no. 7, pp. 4195–4202, 2023.

[28] F. Liu, S. Li, X. Dong, Z. Wang, J. Xiang, D. Li, and Z. Tu, "Design, modelling, and experimental validation of a self-rotating flapping wing rotorcraft with motor–spring resonance actuation system," *Bioinspiration & Biomimetics*, vol. 18, no. 4, p. 046019, 2023.

[29] S. Bai and P. Chirarattananon, "Design and take-off flight of a samara-inspired revolving-wing robot," in *2019 IEEE/RSJ International Conference on Intelligent Robots and Systems (IROS)*. IEEE, 2019, pp. 6070–6076.

[30] H. Zhang, E. Lerner, B. Cheng, and J. Zhao, "Compliant bistable grippers enable passive perching for micro aerial vehicles," *IEEE/ASME Transactions on Mechatronics*, vol. 26, no. 5, pp. 2316–2326, 2020.

[31] J. Weakly, X. Li, T. Agarwal, M. Li, S. Folk, C. Jiang, and C. Sung, "Bistable aerial transformer: A quadrotor fixed-wing hybrid that morphs dynamically via passive soft mechanism," *Journal of Mechanisms and Robotics*, vol. 16, no. 7, p. 071016, 2024.

[32] S. Bai, R. Ding, and P. Chirarattananon, "A micro aircraft with passive variable-sweep wings," *IEEE Robotics and Automation Letters*, vol. 7, no. 2, pp. 4016–4023, 2022.

[33] G. J. Ducard and M. Allenspach, "Review of designs and flight control techniques of hybrid and convertible vtol uavs," *Aerospace Science and Technology*, vol. 118, p. 107035, 2021.

[34] B. Li, J. Sun, W. Zhou, C.-Y. Wen, K. H. Low, and C.-K. Chen, "Transition optimization for a vtol tail-sitter uav," *IEEE/ASME transactions on mechatronics*, vol. 25, no. 5, pp. 2534–2545, 2020.

[35] V. S. Chipade, M. Kothari, R. R. Chaudhari *et al.*, "Systematic design methodology for development and flight testing of a variable pitch quadrotor biplane vtol uav for payload delivery," *Mechatronics*, vol. 55, pp. 94–114, 2018.

[36] C. Bogdanowicz, V. Hrishikeshavan, and I. Chopra, "Development of a quad-rotor biplane mav with enhanced roll control authority in fixed

wing mode," in *Proceedings of the American Helicopter Society, 71st Annual Forum, Virginia Beach, VA, USA*, 2015, pp. 5–7.
[37] Y. Wu, X. Du, R. Duivenvoorden, and J. Kelly, "The phoenix drone: An open-source dual-rotor tail-sitter platform for research and education," in *2019 International Conference on Robotics and Automation (ICRA)*. IEEE, 2019, pp. 5330–5336.
[38] A. N. De Lucena, B. M. F. Da Silva, and L. M. G. Gonçalves, "Double hybrid tailsitter unmanned aerial vehicle with vertical takeoff and landing," *IEEE Access*, vol. 10, pp. 32 938–32 953, 2022.
[39] Y. Yang, J. Zhu, X. Zhang, and X. Wang, "Active disturbance rejection control of a flying-wing tailsitter in hover flight," in *2018 IEEE/RSJ International Conference on Intelligent Robots and Systems (IROS)*. IEEE, 2018, pp. 6390–6396.
[40] R. Ritz and R. D'Andrea, "A global controller for flying wing tailsitter vehicles," in *2017 IEEE international conference on robotics and automation (ICRA)*. IEEE, 2017, pp. 2731–2738.
[41] S. M. Nogar and C. M. Kroninger, "Development of a hybrid micro air vehicle capable of controlled transition," *IEEE Robotics and Automation Letters*, vol. 3, no. 3, pp. 2269–2276, 2018.
[42] S. Li, F. Liu, Y. Gao, J. Xiang, Z. Tu, and D. Li, "Airtwins: Modular bicopters capable of splitting from their combined quadcopter in midair," *IEEE Robotics and Automation Letters*, 2023.
[43] M. Keennon, K. Klingebiel, and H. Won, "Development of the nano hummingbird: A tailless flapping wing micro air vehicle," in *50th AIAA aerospace sciences meeting including the new horizons forum and aerospace exposition*, 2012, p. 588.
[44] Z. Tu, F. Fei, J. Zhang, and X. Deng, "An at-scale tailless flapping-wing hummingbird robot. i. design, optimization, and experimental validation," *IEEE Transactions on Robotics*, vol. 36, no. 5, pp. 1511–1525, 2020.
[45] Z. Tu, F. Fei, L. Liu, Y. Zhou, and X. Deng, "Flying with damaged wings: The effect on flight capacity and bio-inspired coping strategies of a flapping wing robot," *IEEE Robotics and Automation Letters*, vol. 6, no. 2, pp. 2114–2121, 2021.
[46] R. B. Bramlette, T. A. Johnston, and R. M. Barrett-Gonzalez, "Design, construction, and flight testing of the world's fastest micro-scale quadcopter," in *55th AIAA Aerospace Sciences Meeting*, 2017, p. 0012.
[47] M. Karásek, F. T. Muijres, C. De Wagter, B. D. Remes, and G. C. De Croon, "A tailless aerial robotic flapper reveals that flies use torque coupling in rapid banked turns," *Science*, vol. 361, no. 6407, pp. 1089–1094, 2018.
[48] H. V. Phan, S. Aurecianus, T. K. L. Au, T. Kang, and H. C. Park, "Towards the long-endurance flight of an insect-inspired, tailless, two-winged, flapping-wing flying robot," *IEEE Robotics and Automation Letters*, vol. 5, no. 4, pp. 5059–5066, 2020.
[49] Y.-W. Chin, J. M. Kok, Y.-Q. Zhu, W.-L. Chan, J. S. Chahl, B. C. Khoo, and G.-K. Lau, "Efficient flapping wing drone arrests high-speed flight using post-stall soaring," *Science Robotics*, vol. 5, no. 44, p. eaba2386, 2020.
[50] C. De Wagter, R. Ruijsink, E. J. Smeur, K. G. van Hecke, F. van Tienen, E. van der Horst, and B. D. Remes, "Design, control, and visual navigation of the delftacopter vtol tail-sitter uav," *Journal of Field Robotics*, vol. 35, no. 6, pp. 937–960, 2018.
[51] H. Gu, X. Cai, J. Zhou, Z. Li, S. Shen, and F. Zhang, "A coordinate descent method for multidisciplinary design optimization of electric-powered winged uavs," in *2018 International Conference on Unmanned Aircraft Systems (ICUAS)*. IEEE, 2018, pp. 1189–1198.
[52] R. D'Sa and N. Papanikolopoulos, "Design and experiments for multi-section-transformable (mist)-uav," in *2019 International Conference on Robotics and Automation (ICRA)*. IEEE, 2019, pp. 1878–1883.
[53] J. Wang, Y. Tang, Y. Ge, C. Wu, H. Tang, T. Hu, L. Wang, Y. Wang, C. Jiang, Q. Qu *et al.*, "Vectored-thrust system design for a tail-sitter micro-aerial-vehicle with belly/back takeoff ability," *Aerospace Science and Technology*, vol. 155, p. 109542, 2024.
[54] E. Livne and T. A. Weisshaar, "Aeroelasticity of nonconventional airplane configurations-past and future," *Journal of aircraft*, vol. 40, no. 6, pp. 1047–1065, 2003.
[55] S. Bai, Q. Pan, R. Ding, H. Jia, Z. Yang, and P. Chirarattananon, "An agile monopedal hopping quadcopter with synergistic hybrid locomotion," *Science Robotics*, vol. 9, no. 89, p. eadi8912, 2024.
[56] J. D. Anderson, John D., *Fundamentals of aerodynamics*, sixth edition. ed. New York, NY: McGraw-Hill Education, 2017.

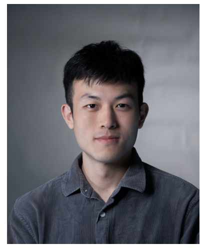

Ruihan Jia received the B.E. degree in mechatronic engineering from the University of Sydney, NSW, Australia, in 2023.

He is currently working toward the M.Phil. degree in the Department of Biomedical Engineering, City University of Hong Kong, Hong Kong SAR, China. His research interests include micro aerial vehicles, dynamics, and robotic perception.

Songnan Bai received the B.S. degree in mechanical engineering from Xi'an Jiaotong University, Xi'an, China, in 2017, the M.Sc. in Mechanical Engineering from City University of Hong Kong, Hong Kong SAR and Ph.D. degree in Biomedical Engineering from City University of Hong Kong, Hong Kong SAR.

He is currently a postdoc fellow in the Department of Biomedical Engineering, City University of Hong Kong, Hong Kong SAR.

Song Li received the B.S. degree in aerospace engineering from Xi'an Jiaotong University, Shaanxi, China, in 2020, and the M.Eng. degree from Beihang University, Beijing, China, in 2023.

He is currently working towards a Ph.D degree in the Department of Biomedical Engineering at City University of Hong Kong, Hong Kong SAR, China.

His research interests include bio-inspired robots, micro air vehicles, flapping-wing robots, and flapping-wing aerodynamics.

Fangzheng Wang received the B.E. degree in Vehicle Engineering from Southwest University, Chongging, China, in 2021 and the M.S. degree in Humam and Biological Robotics from Imperial College London, London, the United Kingdom, in 2022. He is currently working toward the M.Phil. degree in biomedical engineering with the City University of Hong Kong, Hong Kong.

His research interests include water skipping unmanned aerial vehicle.

Hongqiang Wang (Senior Member, IEEE) received the B.S. and M.S. degrees in mechanical engineering from the Xi'an Jiao Tong University, Xi'an, China, in 2008 and 2011, respectively, and the Ph.D. degree in precision mechanical engineering from the Tokyo University, Tokyo, Japan, in 2015. He is currently an Associate Professor at the Department of Mechanical and Energy Engineering, Southern University of Science and Technology, Shenzhen, China. His research interests include miniature robotics, novel actuators, new flexible motors, soft robotics, and medical robotics.

Pakpong Chirarattananon (S'12-M'15) received the B.A. degree in Natural Sciences from the University of Cambridge, U.K., in 2009, and the Ph.D. degree in Engineering Sciences from Harvard University, Cambridge, MA, USA, in 2014. He is currently an Associate Professor with the Department of Biomedical Engineering and Department of Mechanical Engineering, City University of Hong Kong, Hong Kong SAR. His research interests include bio-inspired robots, micro air vehicles, locomotion, and the applications of control and dynamics in robotic systems.

Supplementary Materials for
An Aerial Robot Passively Transforming between Hovering and Forward Flight via Aerodynamically Bistable Structure

Ruihan Jia, Songnan Bai, Song Li, Fangzheng Wang, Hongqiang Wang, and Pakpong Chirarattananon

S1. List of Supplementary Videos

Supplementary Movie 1	Overview and Flight Demonstration of Bimodal Aerial Robot
Supplementary Movie 2	Aerodynamically Bistable Structure and Two Flight Modes
Supplementary Movie 3	Outdoor Revolving Flight with Mild Wind
Supplementary Movie 4	Outdoor Revolving Flight with Position Control
Supplementary Movie 5	Midair Transformation from Forward to Revolving Flight
Supplementary Movie 6	Midair Transformation from Revolving to Forward Flight
Supplementary Movie 7	Revolving Flight Endurance Test

S2. Altitude Loss in Revolving-to-Forward Transition

The transition from revolving-to-forward flight consists of two phases: rotational deceleration and subsequent recovery to level flight. To quantify the altitude loss during this transition, we performed dynamic simulations of both phases and compared the results with experimental observations.

A. Rotational deceleration

To model the coupled rotational and altitude dynamics, we begin with the robot with an initial revolving rate of Ω_0, corresponding to its equilibrium hovering speed, immediately after powering off the rotors. Without thrust, the robot decelerates from revolving motion and descend under aerodynamic forces and gravity.

Considering that airflow is mainly induced by revolving and vertical motion, the airflow velocity and inflow angle ϕ can be expressed as:

$$\mathbf{U} = \begin{bmatrix} \Omega r \\ v_z \end{bmatrix} \quad \text{and} \quad \phi = \arctan\frac{v_z}{\Omega r}, \tag{S1}$$

where r is the radial distance from the revolving axis and v_z is the vertical descent speed. The angle of attack shown in Fig. S1B, depends on the the wing's orientation and the airflow direction. Using the blade element method (Fig. S1A), we compute the sectional lift and drag,accounting for local airflow contributions from both axial and tangential motions:

$$\mathrm{d}F_{L,D} = \frac{1}{2}\rho c C_{L,D}||\mathbf{U}||^2\mathrm{d}r. \tag{S2}$$

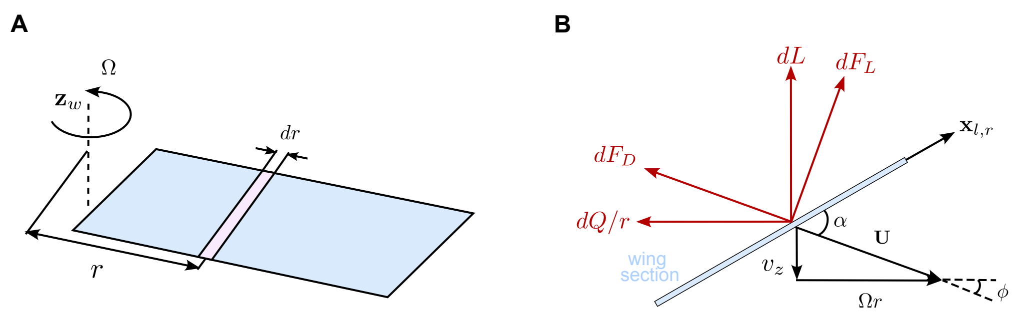

Fig. S1. (A) Application of blade-element momentum theory to a rectangular wing revolving at an angular velocity of Ω. The wing is split into infinitesimally thin blades specified by the spanwise location r and elemental thickness dr. (B) The locally perceived airspeed $\mathbf{U}$ and elemental lift and drag forces on the elemental blade.

The elemental vertical force L and drag torque about the z axis Q, shown in Fig.S1B, are

$$dL = dF_L \cos\phi - dF_D \sin\phi, \tag{S3}$$
$$dQ = -r(dF_L \sin\phi + dF_D \cos\phi). \tag{S4}$$

By integrating these elemental forces along the wing span, the dynamics in yaw and vertical directions can be described as:

$$I_z\dot{\Omega} = 2\int dQ, \tag{S5}$$
$$m\dot{v}_z = 2\int dL - mg, \tag{S6}$$

where I_z is yaw inertia. Based on these equations and physical parameters in Tab. I, the estimated time taken for the robot decelerate the yaw rate from $\Omega_0 = 20$ rad/s to 0 rad/s is 0.53 s. During this deceleration phase, the altitude loss is approximately 0.6 m, with a terminal descent speed of -2.2 m/s.

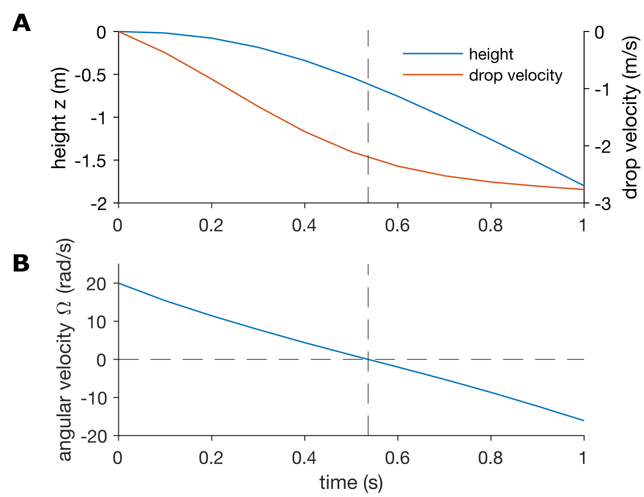

Fig. S2. Simulation results of rotational deceleration. (A) Altitude loss and descent velocity. (B) Yaw rate reduction from $\Omega_0 = 20$ rad/s, with the revolving-wing pitch angle β_w as listed in Table I.

B. Forward acceleration

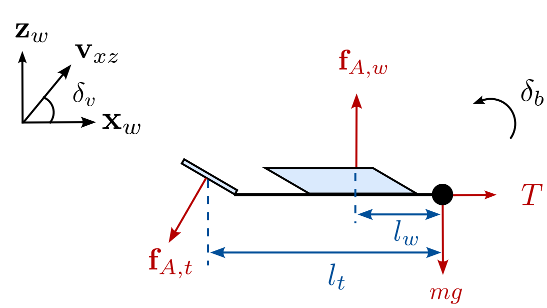

Fig. S3. Diagram of the robot in forward flight mode. Body forces, body pitch angle δ_b, and flight path angle δ_v are labeled.

Once the yaw motion ceases, the transition shifts to pitch rotation and movement in the longitudinal plane. According to Eq. 8, the robot both translates and pitches downward. We assume the left wing flips over and the robot's configuration changes to the forward flight mode immediately after flow direction condition is met. After the mode switching, thrust is activated. Due to its inherent longitudinal stability, the robot eventually achieves equilibrium glide

The longitudinal dynamics in forward flight, with respect to the reference frame (Fig. S3), are

$$m\dot{\mathbf{v}}_{xz} = R_\alpha(\mathbf{T} + 2\mathbf{f}_{A,w} + \mathbf{f}_{A,t}) - \begin{bmatrix} 0 & mg \end{bmatrix}^T, \tag{S7}$$

$$I_y\ddot{\delta}_b = -2l_w \sin\theta f_{A,w} - \frac{l_t}{\cos\beta_t} f_{A,t}, \tag{S8}$$

where $\mathbf{v}_{xz}$ is the velocity in the longitudinal plane, $\mathbf{T}$ is total thrust, θ is the wing sweep angle in level flight, δ_b is the body pitch angle, I_y is the pitch moment of inertia, and l_w is the distance from the CoM to the CoP of the wings in cruising (assumed to be 2.6 cm in simulation). The physical parameters are provided in Table I.

For flat wings, the angle of attack is determined by the interaction between the induced airflow and plate orientation. The inflow velocity for both the wings and tail in the longitudinal plane is influenced by $\mathbf{v}_{xz}$ and body pitch motion $\dot{\delta}_b$:

$$\mathbf{U} = \mathbf{v}_{xz} - l_{w,t}\dot{\delta}_b \mathbf{z}_b, \tag{S9}$$

where $l_{w,t}$ is the distance from the CoM to the wings and tail, and $\mathbf{z}_b$ denotes the body z axis.

In this forward acceleration phase, a simulation shows that with a constant thrust for cruising, the robot converges to a pitch-up flight path within 1.5 s, experiencing an altitude loss of 8.1 m before stabilizing into forward flight. Including the initial 0.6 m descent during rotational deceleration, the total altitude loss during the transition is 8.7 m.

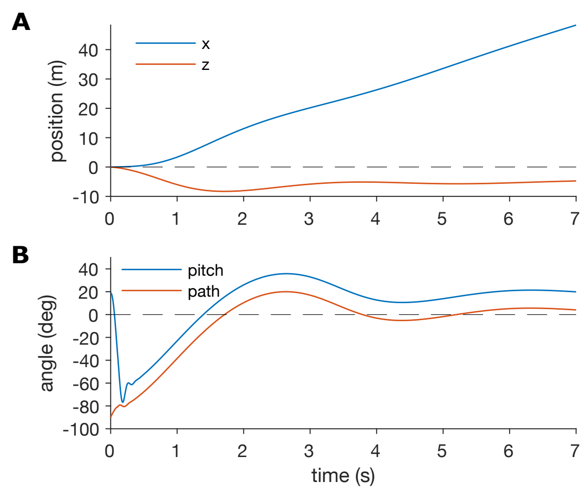

Fig. S4. Simulation result of forward acceleration. (A) position in the longitudinal plane. (B) The robot's pitch angle and flight path angle.

C. Altitude Estimation from Video Footage

In outdoor experiments where ground-truth altitude data is unavailable, video footage can be used for distance estimation. Given that the robot's dimensions remain constant (approx. 65 cm) and near-vertical camera axis, we can estimate height from recorded images. Following the pinhole camera model:

$$d_{\text{img}} = \frac{f}{s} d_{\text{obj}}, \tag{S10}$$

where s is the distance of the object from the camera, d_{img} is the object's dimension in pixel, d_{obj} is its physical dimension, and f is the camera's focal length. The video footage was preprocessed to eliminate lens distortion.

In Fig. S5, the robot's initial altitude was estimated using brick landmarks on a nearby wall (the width of five bricks corresponds to the robot's span diameter) As a result, each blue line in the image represents an equivalent real-world length, though it appears distorted due to perspective effects. In this frame, the robot's span measures 73 pixels, corresponding to the third red-labeled line. Using this reference, the robot's initial altitude is estimated to be at the fourth floor, approximately 16 m above the ground. We note that the camera was positioned approximately 1.8 m above the groundsuch that the distance from the object to the camera s was 14.2 meters.

With constant f and d_{obj}, the robot's atltitude at time i can be determined relative to its altitude at time j using:

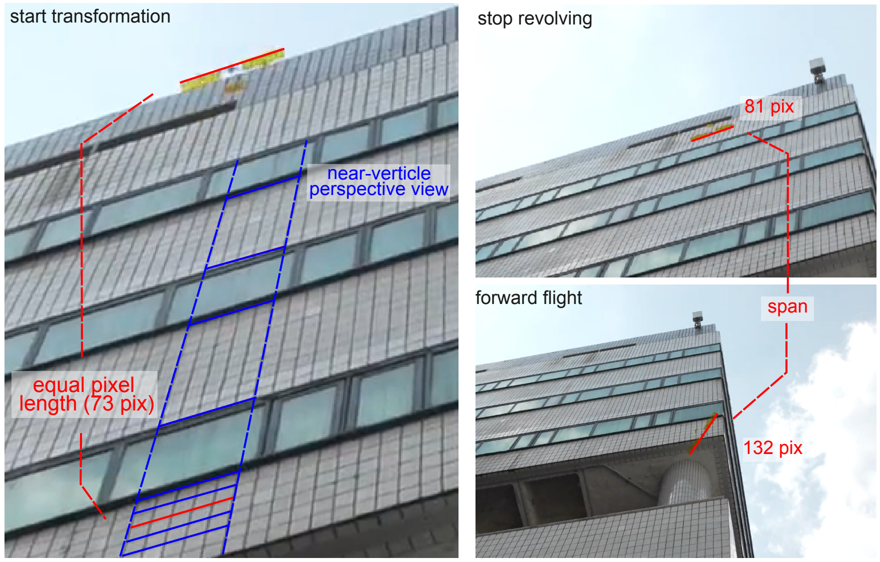

Fig. S5. In the revolving-to-forward transformation, three critical frames were extracted for altitude estimation: start of transformation – estimated altitude: 16 m, stop revolving – estimated altitude: 14.6 m, and forward flight initiation – estimated altitude: 9.6 m.

$$s_i = \frac{d_{\text{img},i}}{d_{\text{img},j}} s_j. \tag{S11}$$

Measured from the frames, the size of the robot is 81 pixels at the moment of revolving stop, and 132 pixels during near-level forward flight. Applying this perspective-based estimation to the rotational deceleration and forward flight stages (as labeled in Fig. S5), the drop height during rotational deceleration was approximately 1.4 m, while the altitude loss during forward acceleration was about 5 m. These values indicate that the robot's altitudes at these locations are 14.6 m and 9.6 m.

Supplementary Figures

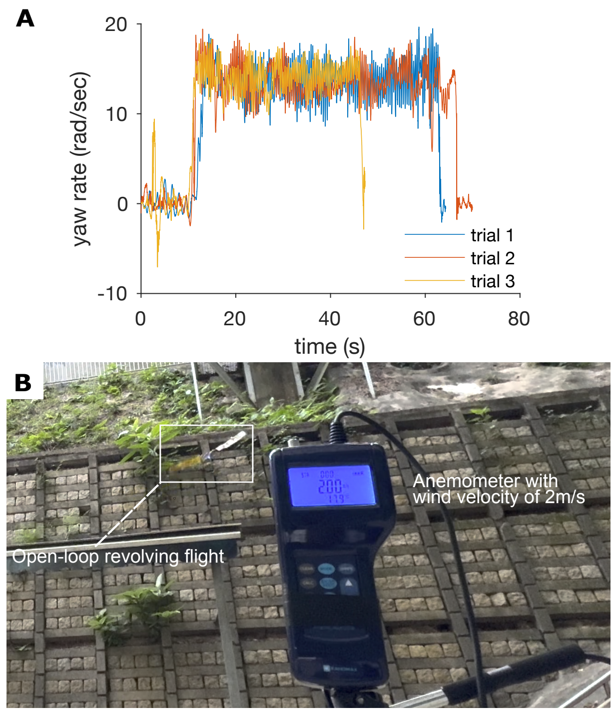

Fig. S6. (A) Yaw rate during revolving flight in moderate wind conditions (0.6-2 m/s). Each hovering interval lasted approximately 40-60 s. (B) Maximum wind speed of 2 m/s recorded by Kanomax 6036 anemometer during robot hovering (Supplementary Movie 3).

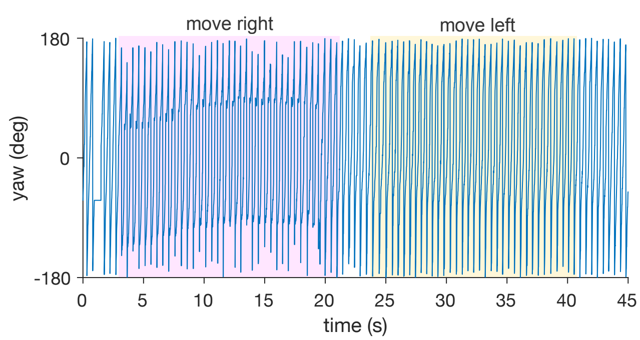

Fig. S7. Plot of yaw angle during revolving flight with horizontal position control.

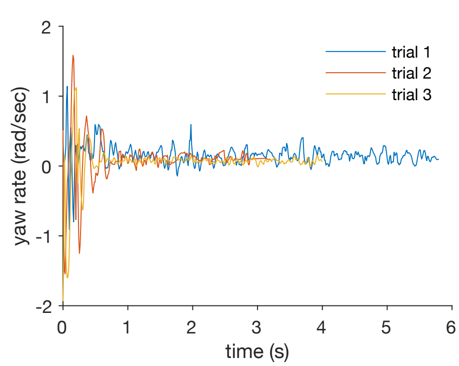

Fig. S8. Plot of yaw rate from three repeated forward flights.

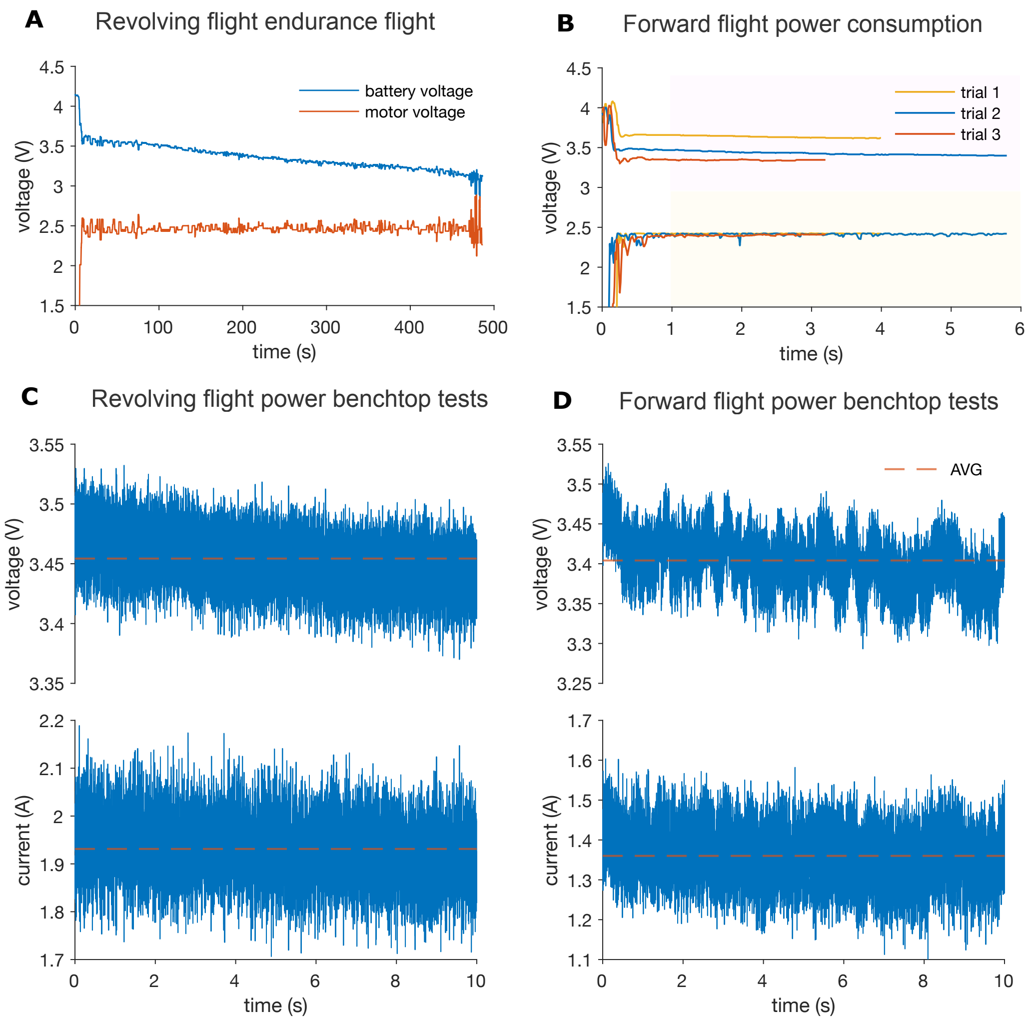

Fig. S9. (A) Battery voltage and average motor voltage during a 478-s revolving endurance test. (B) Average motor voltage during level flight from 4 to 6 s across three trials with different battery conditions. (C) Voltage and current measurements from a benchtop test with the voltage command for revolving-wing hovering. The recorded averages are 3.45 V and 1.93 A. (D) Voltage and current measurements from a benchtop test with the voltage command for forward level flight. The recorded averages are 3.40 V and 1.36 A.

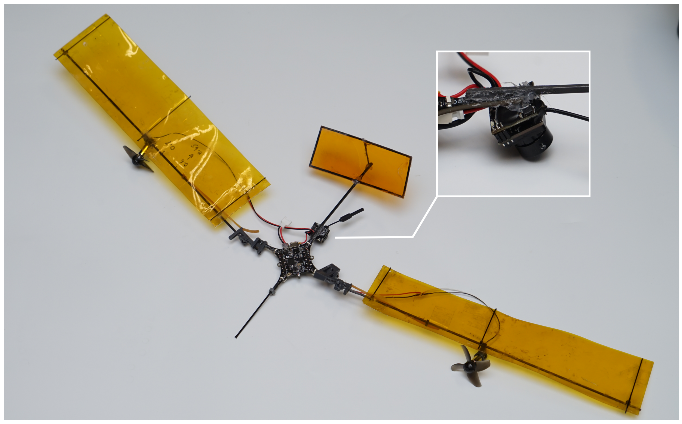

Fig. S10. Photo of the robot equipped with a FPV camera. The camera weighs 3.6 g and has a field of view of 120 degs. The video is remotely transmitted to the ground station.

Fig. S11. During revolving flight, a sequence of down-looking camera images transmitted to the ground station continuously captured the human operator on the ground.

TABLE S1
POWER AND ENDURANCE OF HYBRID MULTIMODAL ROBOTS AND SUB-100-G MAVS

Robot	Number of Actuators	Weight (g)	Power Consumption		Endurance	
			Hovering (W)	Forward (W)	Hovering (mins)	Forward (mins)
Multimodal MAVs						
This work	**2**	**47.4**	**6.67**	**4.63**	**8.0**	-
Three-mode UAV [6]	5	600	96.9	114.4	-	-
DelftaCopter [50]	6	4300	420	300	20	-
Bistable Aerial Transformer [31]	4	1350	491.9	434.6	3.1	-
A Quadrotor Tail-sitter [51]	6	1600	325.97	75.67	8.2	56.0
MIST-UAV [52]	11	2300	346.1	297.9	-	-
A Vectored-thrust MAV [53]	4	300	50	25	-	-
Sub-100-g MAVs						
Revolving-wing Drone 250mAh [26]	2	35.1	4.39	-	14.9	-
Revolving-wing Drone 650mAh [26]	2	42.8	5.81	-	24.5	-
Crazyflie 2.1 [26]	4	32.1	7.57	-	6.3	-
Delfly Nimble [47]	3	28.2	5.64	-	5	-
X-winged Ornithopter [49]	4	27.5	4.8	-	-	-
Nano Hummingbird [43]	4	19	3.27	-	4	-
KUBeetle-S [48]	4	15.8	3.44	-	8.8	-
XQ-139µ QuadSparrow [46]	4	20	3.75	-	8	-
Purdue Hummingbird [44], [45]	2	12.5	5.05	-	-	-